# Shear behavior of a shear thickening fluid-impregnated aramid fabrics at high shear rate

Wonjin Na[1)], Hyunchul Ahn[1)], Sungjin Han[1)], Philip Harrison[2)], Jong Kyoo Park[3)], Euigyung Jeong[3)] and Woong-Ryeol Yu[1*1)]

[1)] Department of Materials Science and Engineering and Research Institute of Advanced Materials (RIAM), Seoul National University, Seoul 151-742, Republic of Korea
[2)] School of Engineering, University of Glasgow, Glasgow G12 8QQ, United Kingdom
[3)] Agency for Defense Development, Daejeon 305-600, Republic of Korea

**Abstract** Shear-thickening fluid-impregnated aramid (STF-im-AR) fabrics have been manufactured for advanced soft body armor applications for which they provide improved ballistic and stab resistances. It is not yet clear whether or not such improvements can be attributed solely to the STF. In this study, the rate-dependent behavior of an STF-im-AR fabric was investigated at the fabric level, using uniaxial tensile, bias-extension, and picture-frame tests. Rate-dependent behavior of the STF-im-AR fabric was observed during uniaxial tensile testing; however, the effect of the STF treatment was slight and consistent with only the inherent effect of the polymeric nature of its constituent fibers. The shear rigidity of the STF-im-AR fabric increased, due to the presence of the STF and the sensitivity of the fabric's shear stiffness to changes in the shear strain rate also increased slightly. This rate-sensitive shear stiffness of STF-im-AR fabrics may contribute to improved ballistic and stab resistances.

*Keywords*: A. Aramid fibre; A. Fabrics/textiles; B. Mechanical properties; Shear-thickening fluid

* Corresponding author. Email : woongryu@snu.ac.kr, Tel. : +82 2 880 9096; Fax : +82 2 883 8197

## 1. Introduction

Woven fabrics made of high-performance fibers, such as aramid (for example, Kevlar) or ultra-high molecular weight polyethylene, have been used in many protective applications, including ballistic and stab body armors [1, 2]. These fibers have been chosen as soft body armor materials mainly due to their high strengths, light weights, flexibility, and heat resistances, which provide better mobility and protection, particularly in military applications [3-5]. The agility and mobility of soldiers wearing such soft armor depend on the performance-to-weight ratio of the materials. Especially polyamide fibers (aramid fibers), which have strong primary (the amide bonding in single fiber chain) and secondary bonding (hydrogen bonding between the fiber chains) in molecular structure, are used for soft armor applications due to the high strength and toughness [6-12]. Thus, many studies have focused on improving the fiber properties, in particular stiffness and strength [13, 14] and heat resistance [15]. On the other hand, the effect of fabric structure, including textile laminating and stitch pattern [16-22], weaving pattern (and resulting elastic properties) [23, 24], and uncertainty of textile [25], on ballistic and stab resistance have been investigated to design the soft body armor. Although these endeavors have improved the bullet and stab resistance of soft body armor, further improvement is still needed. One approach is to consider other functional materials, such as those developed through nanotechnology.

A shear-thickening fluid (STF) is one of these materials [26-28]. Shear-thickening behavior refers to a non-Newtonian fluid phenomenon, i.e., the viscosity increases with the shear strain rate. This behavior is frequently observed in dense suspensions [29-31]; an STF consisting of a suspension of nanoparticles has been reported [29]. When nanoparticles are included in a suspension at high volume fractions, the suspended colloidal particles can form hydroclusters when subject to high shear stresses, leading to

highly viscous and even solid-like behaviour [7, 30]. In previous works, STF-impregnated aramid (STF-im-AR) fabrics were manufactured, demonstrating enhanced stab and ballistic resistance [7, 22, 26, 32]. Experimental research has suggested many cooperative mechanisms to explain the improvement during penetration testing [14, 33], reporting that STF-im-AR fabrics can disperse the absorbed energy through yarn rotation, lateral sliding, uncrimping, translation, plastic deformation and fracture. Based on these fundamental considerations of STF, attempts have been made to design optimized soft fabric body armor using experimental studies including yarn pull-out test, bulletproof test, and conventional impact test [20, 22, 34-40]. Finite element analysis was also carried out to analyse the mechanical behaviour of soft fabric body armor at high shear strain rate, which cannot be observed in experiment. Quantification of the STF effect, however, was not carried out in those studies. The STF effect has been quantified from yarn pull-out tests of STF-im-AR fabrics where the pulling force was measured. A clear enhancement of the pull-out force of a single yarn at pulling rates in the 1–1,000 mm/min range was reported [22, 41, 42]. The maximum pull-out force increased sharply beyond a certain pulling rate (the critical pulling rate). These critical pulling rates increased as the silica nanoparticle content in the STF increased. STF-im-AR fabrics have demonstrated encouraging results such as enhanced energy dissipation and stab and ballistic resistances; however, the mechanism behind such improvement, in particular at the fabric level, requires clarification.

In this study, the effect of an STF on the rate-dependent behavior of AR fabrics was investigated using uniaxial tensile (UT) and shear tests. The measurement range was determined directly from the machine crosshead travel rate, as the tensile strain rate is directly related to the crosshead speed of the tensile test machine. In contrast, during fabric shear tests such as the picture-frame (PF) test, the shear strain rate is determined

by both the crosshead speed and fabric specimen size. Bias-extension (BE) tests were also carried out as they enabled testing at higher shear strain rates than the PF tests.

## 2. Experimental

### *2.1. Materials*

The STF was prepared by dispersing silica nanoparticles (provided as a methanol suspension) in polyethylene glycol (PEG). The silica nanoparticles were spherical with an average diameter of 84 nm. PEG (molecular weight: 200) was chosen as the dispersant because it was less volatile at low temperatures and thus would minimize aging. The silica sol was mixed with PEG using a homogenizer to make a suspension with a silica content of 65 wt% (i.e., 65 wt% silica and 35 wt% PEG), after removing the methanol dispersant via drying in a vacuum oven over a 12 h period. The extent of STF impregnation was observed after drying using a field-emission scanning electron microscopy (FE-SEM) (JSM7600F, JEOL) up to 3,000 × magnification. The magnifications up to 3,000 × were determined considering the size of fibers and impregnated STF clusters, referring to previous literatures [26, 31].

All fabric specimens were prepared using Heracron HT840 plain woven AR fabric (840 denier, 26.2 yarns per inch, Kolon Corporation, Korea) with an areal density of 200 g/m$^2$. The STF suspension was applied to the AR fabric using a brush. The low viscosity of the STF assisted its penetration into the fabric. The STF-im-AR fabric was compressed at 2 kN/m$^2$ for 10 min. By weighing the STF-im-AR fabric after removing the methanol by drying in vacuum oven, the additional weight of the STF suspension to the fabric was determined as 22 % by measurement. The thicknesses of the neat and

STF-im-AR fabrics were 0.28 and 0.31 mm, respectively. The fabrics were cut into test specimens using a laser cutter (JG-10060, K2 laser system, Korea).

### *2.2. Characterization*

#### *2.2.1 Rheological characterization of the STFs*

The rheological behaviors of the STFs were characterized using a stress-controlled rheometer (AR 2000, TA Instruments). The rheological data were obtained in the shear rate sweep mode (from 0.1–$10^4$ $s^{-1}$) at room temperature. The measurement was stopped when the shear stress reached the maximum limit of the instrument ($10^5$ Pa). A cone-and-plate geometry was used (cone angle: 1°; plate diameter: 20 mm). Three STF suspensions (55, 60 and 65 wt% of silica particles in PEG) were characterized.

#### *2.2.2 Uniaxial tensile testing of the STF-im-AR fabric*

UT testing of the STF-im-AR fabric was carried out in accordance with the standard ASTM D5034; five specimens were tested for each test condition. Note that this uniaxial tensile test and other tests with STF impregnated fabric were performed under room temperature, considering the effect of temperature to STF viscosity. The fiber direction was aligned with the loading direction. Note that the fiber direction in woven fabrics means the warp and weft directions. Even though the yarns have waviness (undulations), the yarns can be aligned in the straight direction by viewing them above the top of fabric. Cuts perpendicular to the loading direction were introduced at the center of a fabric specimen, making a narrow test region (Figure 1).

The tensile test was performed using two types of tensile testing machines: an Instron 8801 (Instron, maximum crosshead speed: 1,000 mm/min) and a Zwick Z2.0 (Zwick/Roell, maximum crosshead speed: 15,000 mm/min). For relatively low crosshead speeds, 10/100/1,000 mm/min, the Instron 8801, equipped with a 100 kN load cell and automatic hydraulic parallel grips, was used. For high speed tests, 5,000/10,000/15,000 mm/min, the Zwick Z2.0 with a 2 kN load cell and mechanical parallel grips was used. Each end of the fabric specimen was gripped over a 30 mm length; the gauge length was 100 mm. The tensile load was measured and normalized by the width of the gauge region of the fabric (10 mm), while the strain was measured using a high-speed camera tracing two points marked on the fabric specimen. The neat AR fabric was tested using the same method for comparison.

### *2.2.3 Bias-extension and picture-frame shear testing of the STF-im-AR fabric*

The shear properties of the STF-im-AR fabric were determined using the BE and PF tests [43-46]. The BE test specimens were I-shaped (Figure 2). The fiber direction of a specimen was aligned 45° with respect to the loading direction. To induce pure shear deformation in the center of the testing region, the height/width ratio of a testing specimen, $\lambda$, was set at 2/1. The height of the clamping area was the same as the width of the test specimen, while the width of the clamped region was three times that of the width of the test specimen. The BE test was performed using both test machines described in Section 2.2.2. For the Instron 8801 machine, the crosshead speed was set to 100/500/1,000 mm/min, while higher crosshead speeds (5,000/10,000/15,000 mm/min) were achieved using the Zwick Z2.0 machine. The specimen was marked to measure changes in the fiber angle during the BE test (Figure 2(b)). A high-speed camera

recorded the entire test procedure at a rate of 120 frames per second. The images from the recorded movies were analyzed using ImageJ freeware [http://imagej.nih.gov/ij/] with which the fiber angles were measured every 0.05 s. The neat AR fabric was also tested for comparison.

Cruciform specimens were prepared for the PF shear tests (Figure 3). The specimen consisted of a main rectangular region and four clamping regions. The fiber direction was orientated at 45° with respect to the loading direction. PF tests were performed using the same test machines as used to conduct the BE tests. The crosshead speed conditions for each machine were also set to 100/500/1,000 mm/min and 5,000/10,000/15,000 mm/min for the Instron 8801 and Zwick Z2.0, respectively. A special picture frame was constructed to hold the specimen in the machine. The picture frame consists of four bar (with the same length of 130 mm) linkages and bearings (see Figure 3 (c)). Holes were introduced to the bars to hold the fabric using bolts [43]. The specimen was marked to measure changes in the fiber angle using a high-speed camera (Figure 3(b)).

### 2.3 Normalization of the shear test data

The reaction force, crosshead displacement, speed and fiber angle data were obtained from the BE and PF shear tests. Normalization of the data was required to reveal the shear properties of the STF-im-AR fabric, independent of the specimen size and test method. By considering the stress generated by deforming a sample, Harrison et al. [47-49] developed the following approximate normalized shear force, which is suitable for rate-dependent materials tested using the BE test method:

$$F_{be} = \frac{F_{sh}(\theta)\cdot(2\lambda-3)\cos(\theta)}{(\lambda-1)\left[\cos(\theta/2)-\sin(\theta/2)\right]} + \frac{F_{sh}(\theta/2)\cdot\cos(\theta/2)}{(2\lambda-3)\left[\cos(\theta/2)-\sin(\theta/2)\right]}, \quad (1)$$

where $F_{be}$ is the reaction or axial force measured at the crosshead during the BE test and $\lambda$ is the ratio between the height and width of the test specimen. A detailed explanation of this normalization scheme can be found in [43]. The ideal shear angle in the central region (region A) of the fabric can be calculated from the crosshead displacement using Eq. (2):

$$\theta = \frac{\pi}{2} - 2\arccos\left(\frac{1}{\sqrt{2}} + \frac{d}{\sqrt{2}(\lambda-1)w}\right) \quad (2)$$

where $\theta$ is the shear angle, $d$ is the crosshead displacement, and $w$ is the sample width.

PF test results were normalized simply by dividing by the side length of the PF rig. The axial force was measured and transformed into the shear force per unit length using Eq. (3):

$$F_{sh} = \frac{F_{pf}}{2L_{pf}\cos\varphi}, \quad (3)$$

where $\varphi$ is the frame angle of the picture frame, $F_{pf}$ is the axial reaction force recorded by the tensile testing machine, and $L_{pf}$ is the side length of the PF rig (in this study, the side length of the sample test area and the side length of the PF rig were 130 and 200 mm, respectively). Considering the PF geometry, the shear angle of the fabric, $\theta$, is related to the displacement of the crosshead, $d$, as follows:

$$\theta = \frac{\pi}{2} - 2\cos^{-1}\left(\frac{1}{\sqrt{2}} + \frac{d}{2L_{pf}}\right), \quad (4)$$

Eq. (4) is the theoretical shear angle of the PF test, which is compared with the measured shear angle to assess the deformation behavior of the fabric inside the PF rig.

## 3. Results and discussion

### *3.1. Rheological properties of the STFs*

Figure 4 shows the rheological data for the STFs, i.e., the viscosity and shear stress as a function of the shear strain rate. Strong shear-thickening behavior is apparent from the curves. The onset of shear-thickening shifted to lower shear strain rates when the suspension concentration increased (1,995, 1,000 and 79.4 $s^{-1}$ at 55, 60 and 65 wt%, respectively). The shift of shear-thickening onset can be explained by the clustering mechanism in suspension. The suspension transits from liquid-like state to solid-like state by shear induced aggregation [22, 31, 32]. Increased concentration accelerates the clustering by increasing collisions between particles in same Brownian motion state, resulting in the onset of the shear thickening at lower shear strain rate [50-53]. In all cases, shear-thinning behavior was evident prior to the onset of shear-thickening. In this study, the 65 wt% concentration was selected for the STF used to impregnate the fabric system, due to its moderate viscosity and low onset shear rate for shear-thickening. The shear-thickening effect is observed in the shear stress graphs, i.e., the slope of the shear stress with respect to the shear rate is higher in the shear-thickening region. It was not possible to measure the viscosity of the STF for certain shear rates beyond $10^4$ $s^{-1}$, due to the shear stress capacity limitation of the rheometer ($10^5$ Pa).

SEM images of the STF-*im*-AR fabric are provided in Figure 5. The micrographs demonstrate that the STF had fully impregnated the AR fabric. Figure 5(a)-(c) and (d)-(f)

show the neat and STF-im-AR fabrics, respectively. Even at low resolution, the impregnated state is clearly seen in Figure 5(d). The comparison of high-resolution images of the bundle (Figure 5(b) and (e)) shows more clear impregnation state and the penetration of STF between single fiber. In the single fiber level (Figure 5(c) and (f)), clean (and smooth) neat fiber and bumpy STF-im-AR fiber can be observed, showing clearly the coating state of STF-im-AR fabric.

### *3.2. Uniaxial tensile test results*

The UT test was conducted for the neat and STF-im-AR fabrics (Figure 6). The crosshead speed of the test machine was varied from 10–15,000 mm/min to produce strain rates in the gauge region of the sample that ranged from 0.00166–2.50 $s^{-1}$. The measured forces were normalized by the width of the fabric specimen (instead of by its cross-sectional area). The stress–strain curves were relatively insensitive to strain rate. Mechanical properties including the elastic modulus, tensile strength, and failure strain were investigated (Figure 7). The elastic modulus was measured as the secant modulus in the 0.002–0.010 strain range. The elastic modulus of the STF-im-AR fabric increased with increasing strain rate (Figure 7(a)). This trend was observed for both the neat and STF-im-AR fabrics; however, the minimal difference between these fabrics implied that the rate effect was not caused by the STF. As the strain rate increased, the average tensile strength and failure strain of the fabrics decreased slightly (Figure 7(b) and (c)), although this was not statistically significant. No significant difference was observed between the neat and STF-treated fabrics, confirming that it was not the STF that caused the rate-dependence of the tensile properties of the STF-im-AR fabric. The AR fabric consists of polyamide fibers (aramid). The AR fabric consists of polyamide fibers,

having hydrogen bonding between molecules. It may be possible that hydrogen in amide group and oxygen in PEG can form hydrogen bond considering the chemical structures of these components. The strength of STF-treated AR fabrics decreased, from which we can deduce no interaction between amide group and PEG. On the other hand, penetrated silica nanoparticles can deteriorate the surface of aramid fibers, resulting in the decreased tensile strength [27, 35-37]. As the strain rate increased, silica nanoparticles might cause more scratches, bringing about decreased tensile strength and failure strain. Thus, the rate effects apparent in the tensile response of both fabrics most likely stem from the viscoelastic nature of these fibers.

### *3.3. Shear properties measured using the uniaxial bias-extension test*

The effects of the STF on the fabric shear properties were investigated using the BE test. Figure 8 shows a typical result for both untreated and STF-im-AR fabrics. The crosshead speed ranged from 100–15,000 mm/min, i.e., the shear rates varied from 0.122–3.003 rad/s. The normalized shear force and ideal shear angle were calculated using Eqs. (1) and (2), respectively. To conveniently quantify and interpret the shear force vs. shear angle curves, a bilinear approximation of the curve was used to define two moduli (Slopes 1 and 2) and a knee angle (the transition of the moduli), as shown in Figure 9(a). The knee angle can be used to describe the shear properties of the fabric, because this angle is related to the locking characteristics of the fabric.

Figure 9(b) and (c) demonstrate that both Slopes 1 and 2 increased due to the STF coating; at the same shear angle, the shear force of the STF-im-AR fabric was about three times that of the untreated fabric. This increase was attributed to the effect of the

impregnated silica nanoparticles deposited from the STF suspension that impeded tow and inter-tow shear by increasing friction between the fibers. Note that the nature of Slopes 1 and 2 were determined by deformation mechanism. At low shear strain, the pure shear is dominant (Slope 1 region), however as the shear strain increases, the deformation mode deviates from pure shear [3, 4], i.e., intra-ply slip or yarn jamming become dominant. The gradient of Slope 1 and Slope 2 vs. angular shear rate increased linearly for both the treated and untreated fabrics. The gradient of Slope 2 vs. angular shear rate was slightly different for the two types of fabric (Figure 9(c)), i.e., the two fitted linear lines were not parallel; the increasing Slope 2 of the treated fabric indicates a greater sensitivity to increasing strain rate. The knee angle of the STF-im-AR fabric was lower than that of the AR fabric, and the knee angle in both fabrics decreased with increasing shear strain rate. It is likely that the STF suspension partially filled the space between the fibers or tows, thereby impeding the shear deformation and compaction of the fabric and resulting in a shift of the knee angle due to yarn locking [33, 54, 55]. These results suggest that the shear rigidity of the STF-im-AR fabric increased, due to the presence of the STF and sensitivity to the strain rate.

### *3.4. Picture-frame test results*

Figure 10 shows the normalized shear force vs. ideal shear angle for the untreated and STF-im-AR fabrics as measured by the PF test. The crosshead speed of the tensile machine ranged from 100–15,000 mm/min, applying shear rates to the fabrics of 0.010–1.022 rad/s. These strain rates were smaller than those used in the BE tests, due to the larger specimen geometry used for the PF test. The normalized shear force and shear angle were calculated using Eqs. (3) and (4). The shear rigidity of the STF-im-AR fabric

was higher than that of untreated fabric, confirming the stiffening effect of the silica particles in the PF test.

Similar to the BE test results, the shear force vs. angle curves (Figure 10) for the PF tests could be approximated by bilinear curves and three parameters (Slope 1, Slope 2 and the knee angle) (Figure 11). Slopes 1 and 2 increased linearly with angular shear rate, while the knee angle decreased. The shear rigidity of the STF-im-AR fabric was higher than that of the untreated fabric. These trends were the same as for the BE test. Slopes 1 and 2 of the untreated and STF-im-AR fabrics are parallel to each other; i.e., both fabrics showed a rate dependency, and the STF effect was as evident as with the BE tests (see the low shear strain rate data in Figure 9). The knee angle shown in Figure 11(c) is slightly different for the two fabrics; the linearly decreasing trend of knee angle with angular shear rate of STF-im-AR fabric was slightly more pronounced for the treated fabric than for the untreated fabric. The same explanation as explained in section 3.3 can be also applied to the trend of the knee angle.

Finally, Figure 12 compares the bilinear shear properties of the untreated and STF-im-AR fabrics, measured using the BE and PF tests. Slope 1 and the knee angle measured using the PF tests were smaller than those obtained from the BE tests, while Slope 2 from the two tests was similar. This was attributed to the deformation mechanism of the woven fabrics. The shear behavior involves other forces resulting from the yarn contacts, of which the contribution to the axial force is larger than that of fabric shearing; the shear behavior of woven fabrics after locking is not significantly dependent on the test (PF and BE) [48, 49]. Therefore, Slope 2 was similar for the PF and BE tests. Slope 1, however, represents the shear stiffness of woven fabrics at low shearing angle, i.e., under small deformation. Therefore, Slope 1 can be more influenced

by test boundary conditions or deformation modes (for example, pure shear or simple shear, or yarn straightening) than Slope 2, resulting in differences in Slope 1 for the two tests. Nevertheless, because the trends of Slopes 1 and 2 and knee angle are the same for the two tests in the low shear strain rate regime, it is meaningful to discuss the rate-dependent shear behavior of woven fabrics using these three properties when measured at a high shear strain rate by the BE test.

## 4. Conclusion

The rate-dependent mechanical properties of an STF-im-AR fabric were investigated using UT, BE, and PF tests. Rate-dependent behavior of the tensile properties was observed for both the untreated and STF-im-AR fabrics. This behavior was attributed to the viscoelastic polymeric nature of the constituent fibers. An STF effect was not evident in the tensile properties. A bilinear approximation was made for the normalized shear force vs. the shear angle curves, from which three quantitative parameters of the shear properties (two moduli and the knee angle) were obtained; those three parameters characterized the rate-dependent behavior of the STF-im-AR fabric. The shear resistance of the fabric was enhanced significantly by STF impregnation, especially in Slope 2, after kinematic shear deformation. The observed rate-sensitive shear stiffness of STF-im-AR fabrics may contribute to their improved ballistic and stab resistances.

***Acknowledgement***

This work was supported by Defense Acquisition Program Administration and Agency

for Defense Development under the contract UE135099GD.

## References


[1] Lim CT, Shim VPW, Ng YH. Finite-element modeling of the ballistic impact of fabric armor. International Journal of Impact Engineering. 2003;28(1):13-31.
[2] Li T-T, Wang R, Lou C-W, Lin J-H. Static and dynamic puncture behaviors of compound fabrics with recycled high-performance Kevlar fibers. Composites Part B: Engineering. 2014;59:60-6.
[3] Nilakantan G, Keefe M, Bogetti TA, Gillespie Jr JW. Multiscale modeling of the impact of textile fabrics based on hybrid element analysis. International Journal of Impact Engineering. 2010;37(10):1056-71.
[4] Bresciani LM, Manes A, Ruggiero A, Iannitti G, Giglio M. Experimental tests and numerical modelling of ballistic impacts against Kevlar 29 plain-woven fabrics with an epoxy matrix: Macro-homogeneous and Meso-heterogeneous approaches. Composites Part B: Engineering. 2016;88:114-30.
[5] Mouritz AP. Ballistic impact and explosive blast resistance of stitched composites. Composites Part B: Engineering. 2001;32(5):431-9.
[6] Zhu D, Mobasher B, Rajan S. Dynamic Tensile Testing of Kevlar 49 Fabrics. Journal of Materials in Civil Engineering. 2011;23(3):230-9.
[7] Lee Y, Wetzel ED, Wagner NJ. The ballistic impact characteristics of Kevlar® woven fabrics impregnated with a colloidal shear thickening fluid. Journal of Materials Science. 2003;38(13):2825-33.
[8] Wang Y, Xia Y. The effects of strain rate on the mechanical behaviour of kevlar fibre bundles: an experimental and theoretical study. Composites Part A: Applied Science and Manufacturing. 1998;29(11):1411-5.
[9] Reis PNB, Ferreira JAM, Zhang ZY, Benameur T, Richardson MOW. Impact response of Kevlar composites with nanoclay enhanced epoxy matrix. Composites Part B: Engineering. 2013;46:7-14.
[10] Zhu D, Vaidya A, Mobasher B, Rajan SD. Finite element modeling of ballistic impact on multi-layer Kevlar 49 fabrics. Composites Part B: Engineering. 2014;56:254-62.
[11] Bandaru AK, Vetiyatil L, Ahmad S. The effect of hybridization on the ballistic impact behavior of hybrid composite armors. Composites Part B: Engineering. 2015;76:300-19.
[12] Yan R, Wang R, Lou C-W, Lin J-H. Low-velocity impact and static behaviors of high-resilience thermal-bonding inter/intra-ply hybrid composites. Composites Part B: Engineering. 2015;69:58-68.
[13] Cunniff PM. An Analysis of the System Effects in Woven Fabrics under Ballistic Impact. Textile Research Journal. 1992;62(9):495-509.
[14] Cheeseman BA, Bogetti TA. Ballistic impact into fabric and compliant composite laminates. Composite Structures. 2003;61(1–2):161-73.
[15] Prosser RA, Cohen SH, Segars RA. Heat as a Factor in the Penetration of Cloth Ballistic Panels by 0.22 Caliber Projectiles. Textile Research Journal. 2000;70(8):709-22.
[16] Ahmad MR, Ahmad WYW, Salleh J, Samsuri A. Effect of fabric stitching on ballistic impact resistance of natural rubber coated fabric systems. Materials & Design. 2008;29(7):1353-8.
[17] Kędzierski P, Popławski A, Gieleta R, Morka A, Sławiński G. Experimental and numerical investigation of fabric impact behavior. Composites Part B: Engineering. 2015;69:452-9.
[18] Bazhenov S. Dissipation of energy by bulletproof aramid fabric. Journal of Materials Science. 1997;32(15):4167-73.
[19] Lee BL, Walsh TF, Won ST, Patts HM, Song JW, Mayer AH. Penetration Failure Mechanisms of Armor-Grade Fiber Composites under Impact. Journal of Composite Materials. 2001;35(18):1605-33.
[20] Park JL, Yoon BI, Paik JG, Kang TJ. Ballistic performance of p-aramid fabrics impregnated with shear thickening fluid; Part II – Effect of fabric count and shot location. Textile Research Journal. 2012;82(6):542-57.
[21] Zhou Y, Chen X, Wells G. Influence of yarn gripping on the ballistic performance of woven fabrics from ultra-high molecular weight polyethylene fibre. Composites Part B: Engineering. 2014;62:198-204.
[22] Park JL, Yoon BI, Paik JG, Kang TJ. Ballistic performance of p-aramid fabrics impregnated with shear thickening fluid; Part I – Effect of laminating sequence. Textile Research Journal. 2012;82(6):527-41.
[23] Abu Bakar IA, Kramer O, Bordas S, Rabczuk T. Optimization of elastic properties and weaving patterns of woven composites. Composite Structures. 2013;100:575-91.
[24] Seretis GV, Kostazos PK, Manolakos DE, Provatidis CG. On the mechanical response of woven para-aramid protection fabrics. Composites Part B: Engineering. 2015;79:67-73.
[25] Ilyani Akmar AB, Lahmer T, Bordas SPA, Beex LAA, Rabczuk T. Uncertainty quantification of dry woven fabrics: A sensitivity analysis on material properties. Composite Structures. 2014;116:1-17.
[26] Hassan TA, Rangari VK, Jeelani S. Synthesis, processing and characterization of shear thickening fluid (STF) impregnated fabric composites. Materials Science and Engineering: A. 2010;527(12):2892-9.

[27] Decker MJ, Halbach CJ, Nam CH, Wagner NJ, Wetzel ED. Stab resistance of shear thickening fluid (STF)-treated fabrics. Composites Science and Technology. 2007;67(3–4):565-78.
[28] Lu Z, Wu L, Gu B, Sun B. Numerical simulation of the impact behaviors of shear thickening fluid impregnated warp-knitted spacer fabric. Composites Part B: Engineering. 2015;69:191-200.
[29] Brown E, Forman NA, Orellana CS, Zhang H, Maynor BW, Betts DE, et al. Generality of shear thickening in dense suspensions. Nat Mater. 2010;9(3):220-4.
[30] Lee Y, Wagner N. Dynamic properties of shear thickening colloidal suspensions. Rheol Acta. 2003;42(3):199-208.
[31] Kang T, Hong K, Yoo M. Preparation and properties of fumed silica/Kevlar composite fabrics for application of stab resistant material. Fibers Polym. 2010;11(5):719-24.
[32] Wetzel ED, Lee YS, Egres RG, Kirkwood KM, Kirkwood JE, Wagner NJ. The Effect of Rheological Parameters on the Ballistic Properties of Shear Thickening Fluid (STF)-Kevlar Composites. AIP Conference Proceedings. 2004;712(1):288-93.
[33] Shim VPW, Lim CT, Foo KJ. Dynamic mechanical properties of fabric armour. International Journal of Impact Engineering. 2001;25(1):1-15.
[34] Majumdar A, Butola BS, Srivastava A. Optimal designing of soft body armour materials using shear thickening fluid. Materials & Design. 2013;46:191-8.
[35] Majumdar A, Butola BS, Srivastava A. Development of soft composite materials with improved impact resistance using Kevlar fabric and nano-silica based shear thickening fluid. Materials & Design. 2014;54:295-300.
[36] Park Y, Kim Y, Baluch AH, Kim C-G. Empirical study of the high velocity impact energy absorption characteristics of shear thickening fluid (STF) impregnated Kevlar fabric. International Journal of Impact Engineering. 2014;72:67-74.
[37] Hasanzadeh M, Mottaghitalab V. The Role of Shear-Thickening Fluids (STFs) in Ballistic and Stab-Resistance Improvement of Flexible Armor. J of Materi Eng and Perform. 2014;23(4):1182-96.
[38] Lu Z, Jing X, Sun B, Gu B. Compressive behaviors of warp-knitted spacer fabrics impregnated with shear thickening fluid. Composites Science and Technology. 2013;88:184-9.
[39] Baharvandi HR, Alebooyeh M, Alizadeh M, Heydari MS, Kordani N, Khaksari P. The influences of particle–particle interaction and viscosity of carrier fluid on characteristics of silica and calcium carbonate suspensions-coated Twaron® composite. Journal of Experimental Nanoscience. 2015:1-14.
[40] Gu B. Analytical modeling for the ballistic perforation of planar plain-woven fabric target by projectile. Composites Part B: Engineering. 2003;34(4):361-71.
[41] Kirkwood KM, Kirkwood JE, Young Sil Lee, Egres RG, Wagner NJ, Wetzel ED. Yarn Pull-Out as a Mechanism for Dissipating Ballistic Impact Energy in Kevlar® KM-2 Fabric: Part I: Quasi-Static Characterization of Yarn Pull-Out. Textile Research Journal. 2004;74(10):920-8.
[42] Nilakantan G, Merrill RL, Keefe M, Gillespie Jr JW, Wetzel ED. Experimental investigation of the role of frictional yarn pull-out and windowing on the probabilistic impact response of kevlar fabrics. Composites Part B: Engineering. 2015;68:215-29.
[43] Harrison P, Clifford MJ, Long AC. Shear characterisation of viscous woven textile composites: a comparison between picture frame and bias extension experiments. Composites Science and Technology. 2004;64(10–11):1453-65.
[44] Lebrun G, Bureau MN, Denault J. Evaluation of bias-extension and picture-frame test methods for the measurement of intraply shear properties of PP/glass commingled fabrics. Composite Structures. 2003;61(4):341-52.
[45] Potter K. Bias extension measurements on cross-plied unidirectional prepreg. Composites Part A: Applied Science and Manufacturing. 2002;33(1):63-73.
[46] Chen Q, Boisse P, Park CH, Saouab A, Bréard J. Intra/inter-ply shear behaviors of continuous fiber reinforced thermoplastic composites in thermoforming processes. Composite Structures. 2011;93(7):1692-703.
[47] Härtel F, Harrison P. Evaluation of normalisation methods for uniaxial bias extension tests on engineering fabrics. Composites Part A: Applied Science and Manufacturing. 2014;67:61-9.
[48] Harrison P, Wiggers J, Long AC. Normalization of Shear Test Data for Rate-independent Compressible Fabrics. Journal of Composite Materials. 2008;42(22):2315-44.
[49] Harrison P, Clifford MJ, Long AC, Rudd CD. A constituent-based predictive approach to modelling the rheology of viscous textile composites. Composites Part A: Applied Science and Manufacturing. 2004;35(7–8):915-31.
[50] Bender JW, Wagner NJ. Optical Measurement of the Contributions of Colloidal Forces to the Rheology of Concentrated Suspensions. Journal of Colloid and Interface Science. 1995;172(1):171-84.
[51] Bender J, Wagner NJ. Reversible shear thickening in monodisperse and bidisperse colloidal

dispersions. Journal of Rheology. 1996;40(5):899-916.
[52] Phung TN, Brady JF, Bossis G. Stokesian Dynamics simulation of Brownian suspensions. Journal of Fluid Mechanics. 1996;313:181-207.
[53] Brown E, Jaeger HM. Dynamic Jamming Point for Shear Thickening Suspensions. Physical Review Letters. 2009;103(8):086001.
[54] Song B, Chen W, Weerasooriya T. Quasi-Static and Dynamic Compressive Behaviors of a S-2 Glass/SC15 Composite. Journal of Composite Materials. 2003;37(19):1723-43.
[55] Woo S-C, Kim T-W. High-strain-rate impact in Kevlar-woven composites and fracture analysis using acoustic emission. Composites Part B: Engineering. 2014;60:125-36.

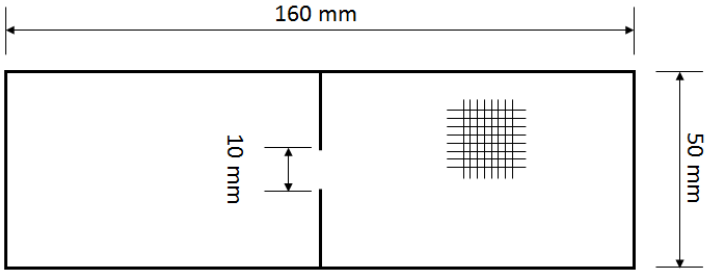


(a)

(b)

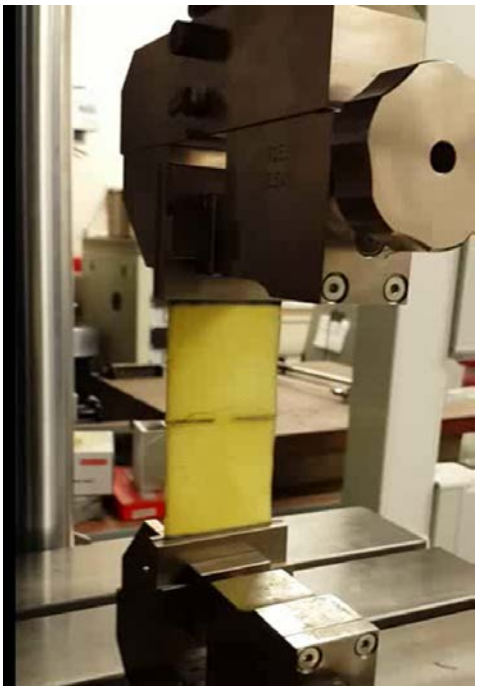

(c)

Figure 1. (a) Specimen geometry and (b) an aramid (AR) fabric specimen used for uniaxial tensile (UT) testing and (c) testing set-up.

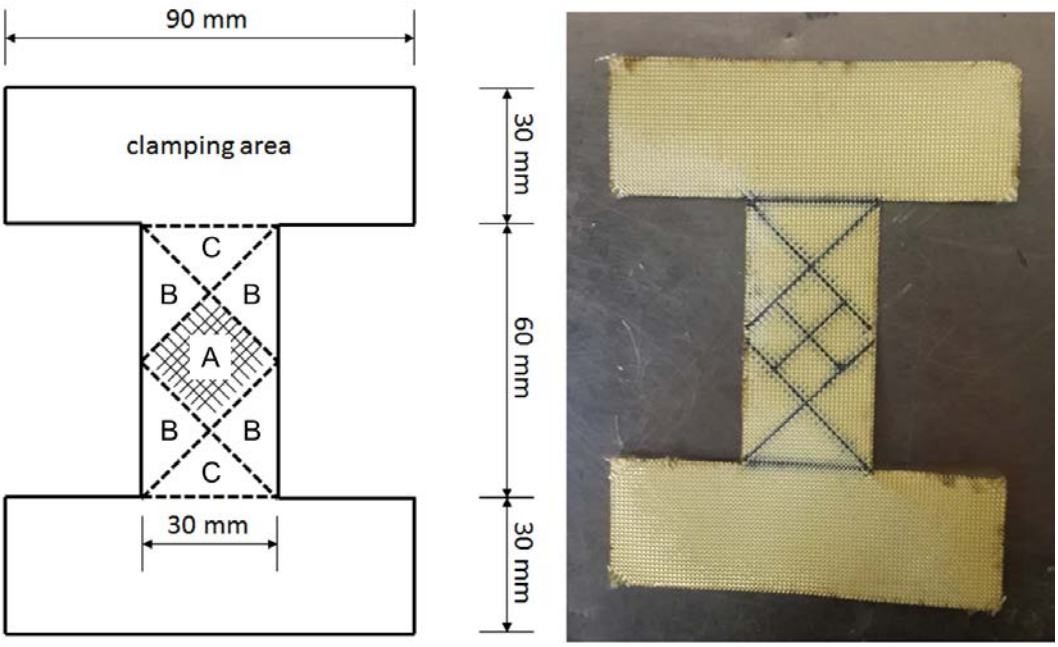


(a) (b)

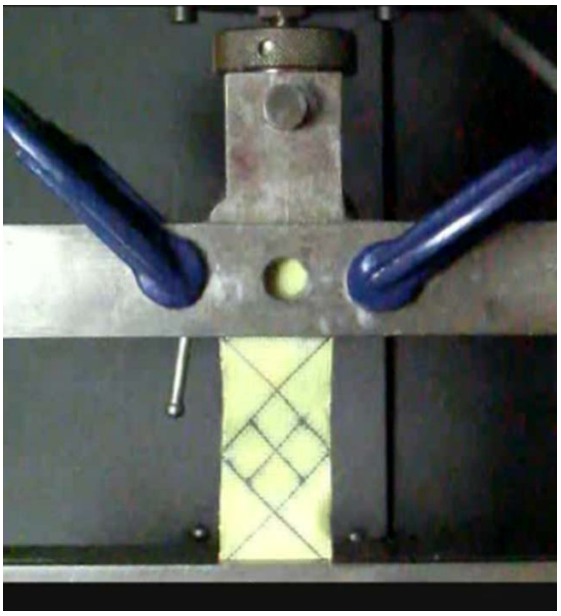

(c)

Figure 2. (a) Specimen geometry and (b) an AR fabric specimen used for bias-extension (BE) shear testing and (c) test set-up.

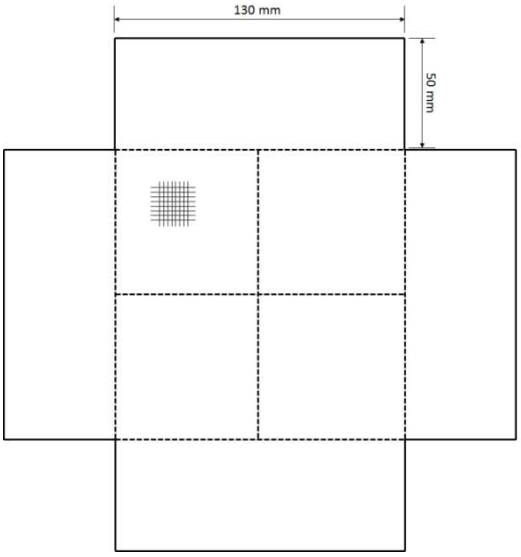


(a)

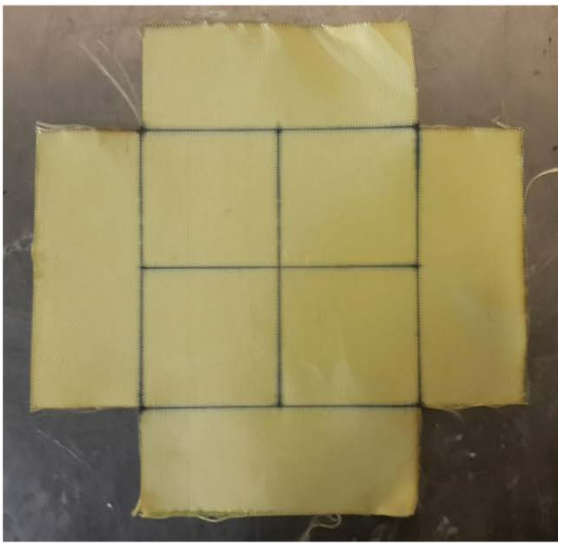

(b)

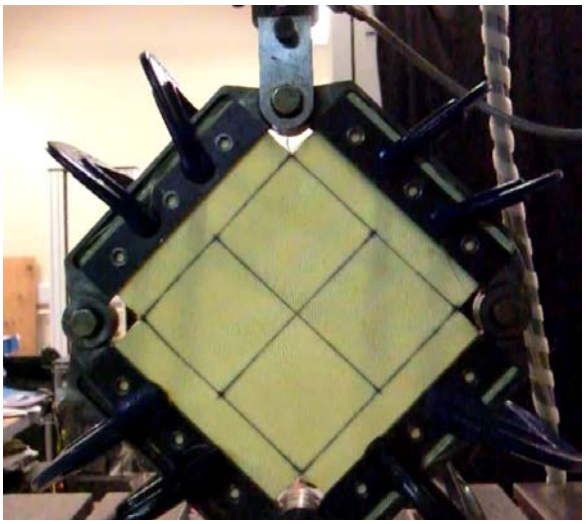

(c)

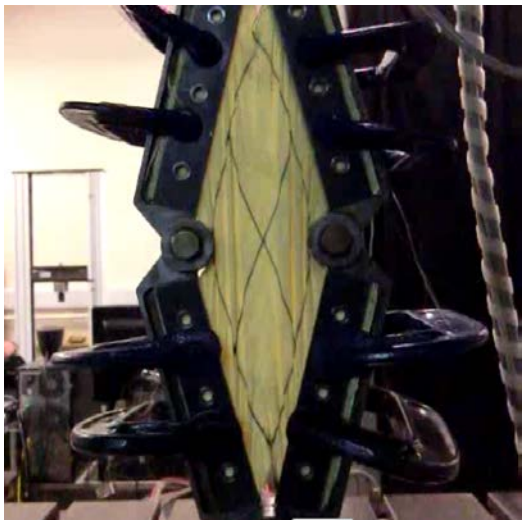

(d)

Figure 3. (a) Specimen geometry and (b) an AR fabric specimen used for picture frame (PF) shear testing. (c) and (d) testing set-ups.

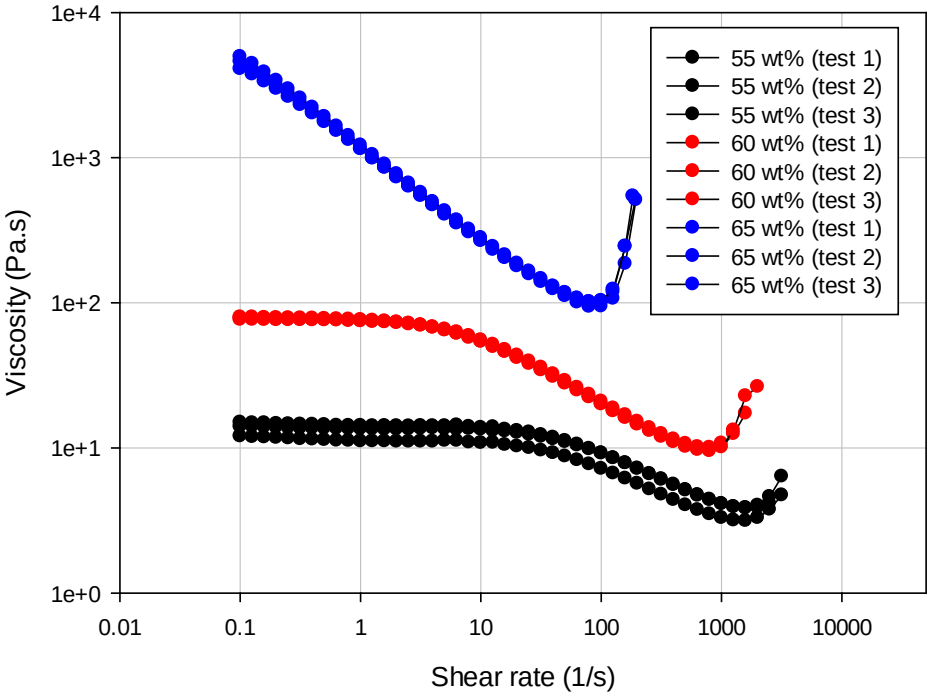


(a)

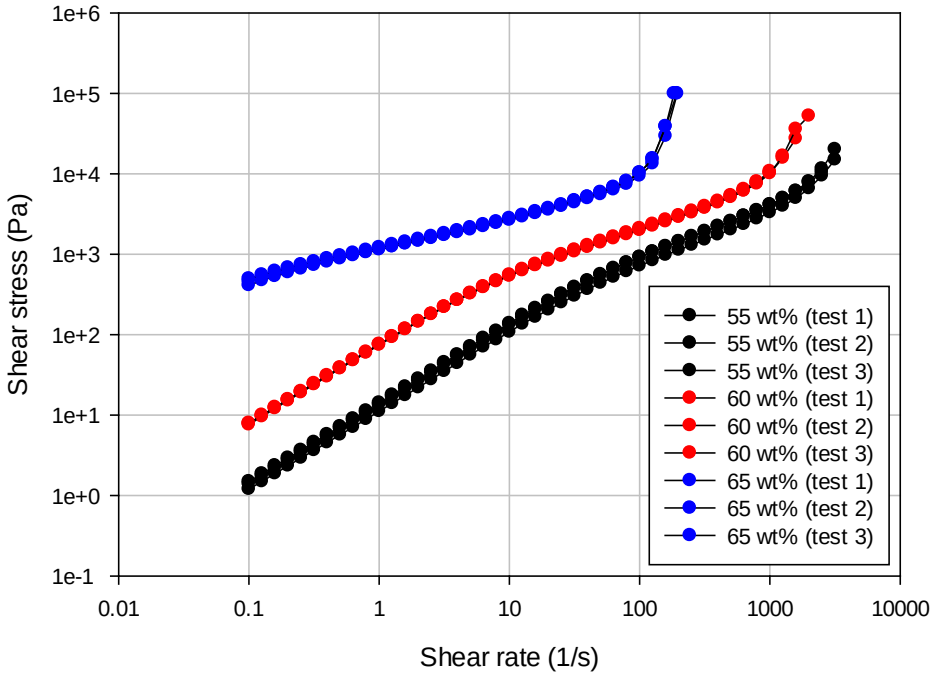


(b)

Figure 4. Rheological characterization of shear-thickening fluids (STFs). (a) Viscosity vs. shear rate curves and (b) shear stress vs. shear rate curve.

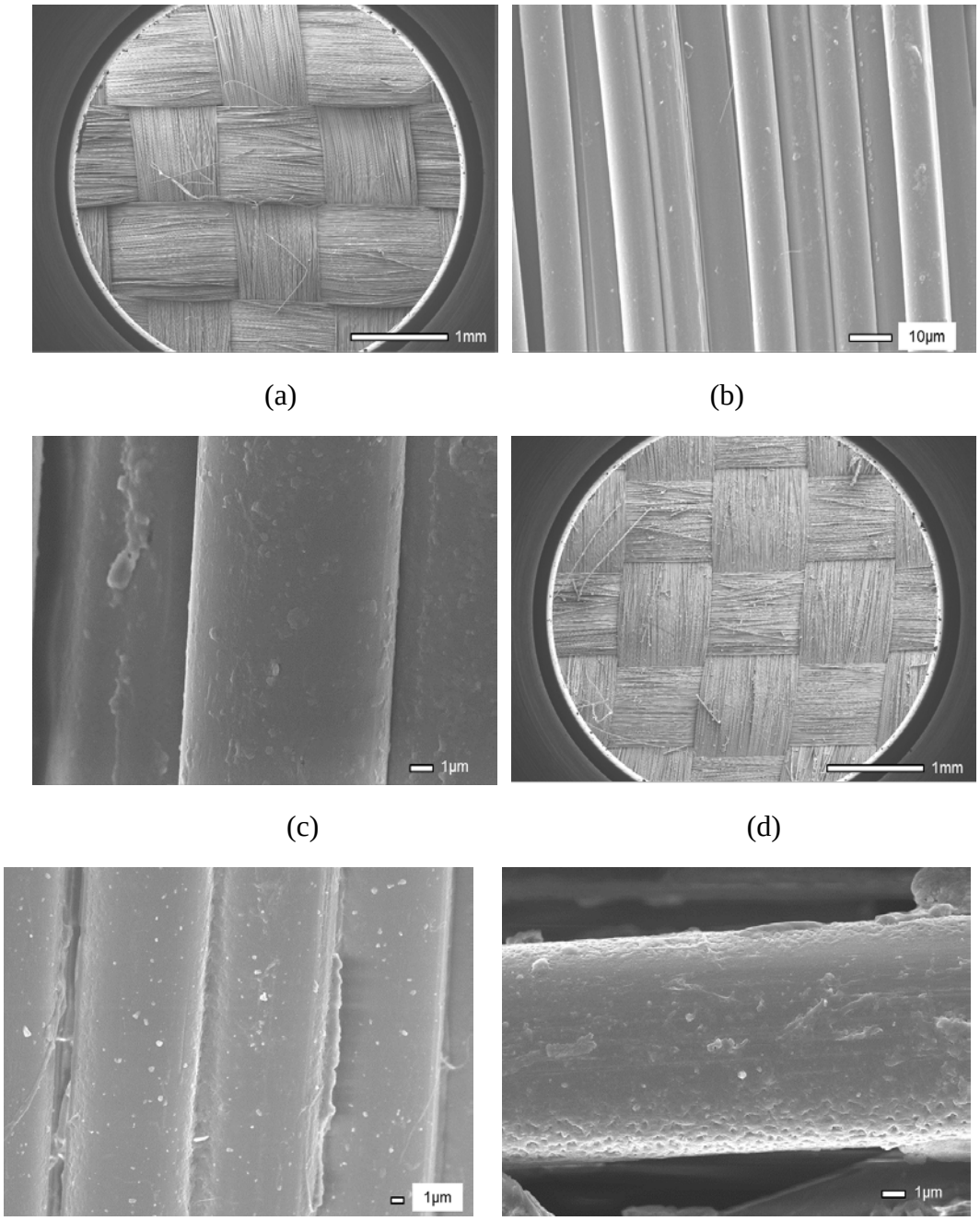


Figure 5. Scanning electron microscopy (SEM) images of the neat and shear-thickening fluid-impregnated aramid (STF-im-AR) fabrics. (a) Overall neat fabric (25×), (b) inside a bundle of individual fibers of (a) (1,000×), (c) a single fiber (5,000×), (d) overall STF-im-AR fabric (25×), (e) inside a bundle of individual fibers of (b) (3,000×), and (f) a single fiber (5,000×)

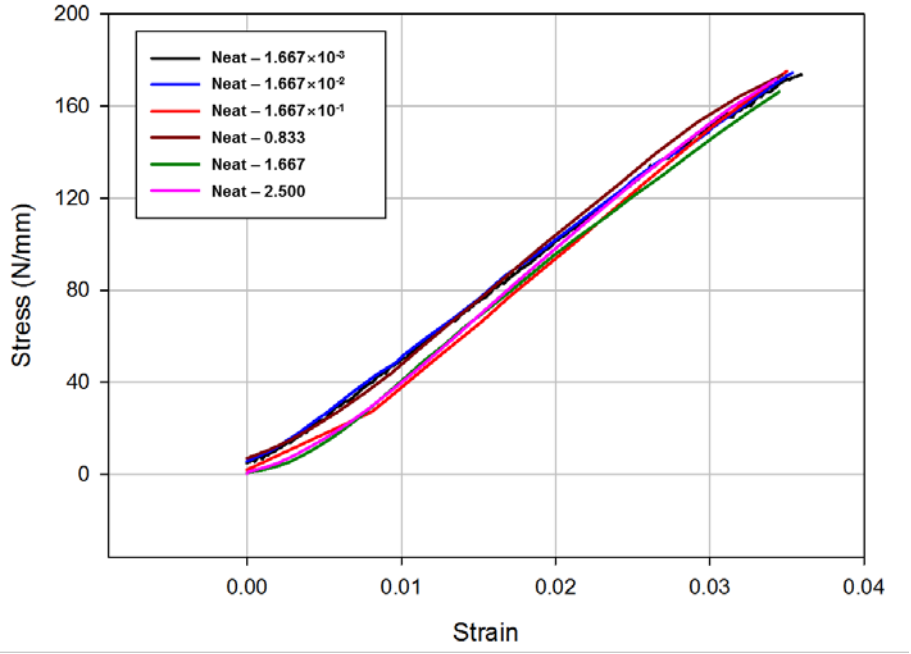


(a)

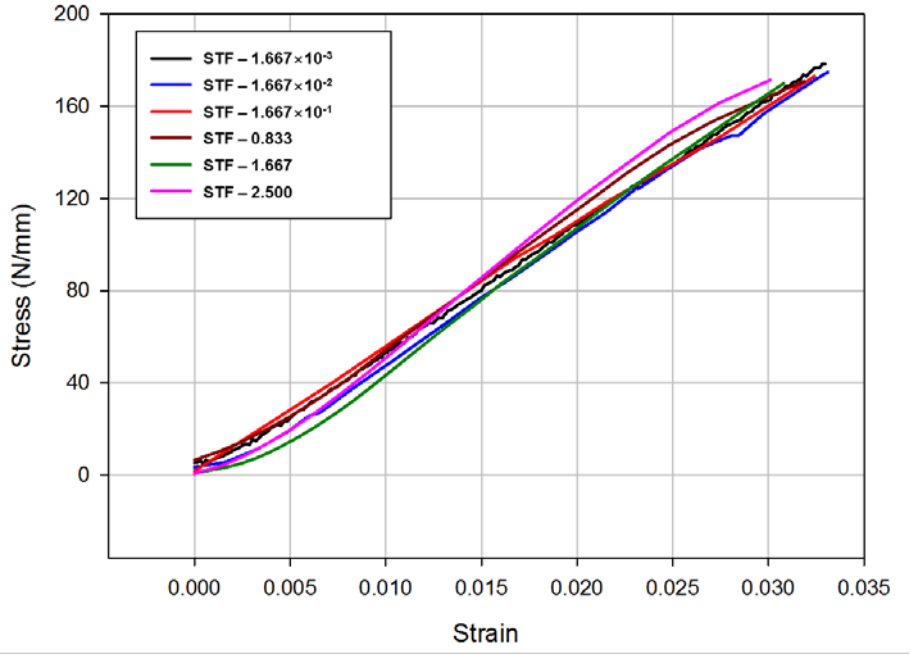


(b)

Figure 6. Stress-strain curves of the fabrics measured using UT test as a function of strain rate. The values in the legends indicate the strain rates. (a) Neat fabric and (b) STF-im-AR fabric.

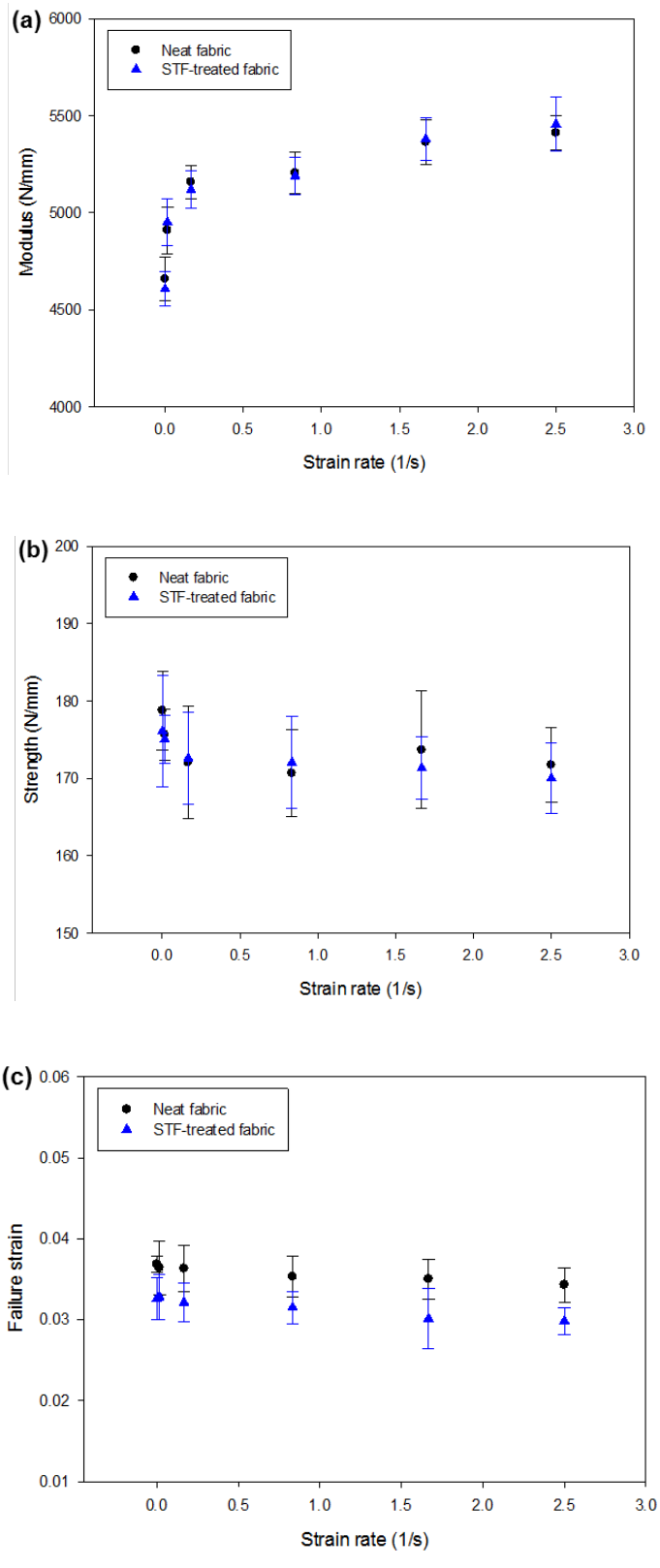


Figure 7. Tensile properties of the neat and STF-im-AR fabrics. (a) Elastic modulus, (b) tensile strength, and (c) failure strain.

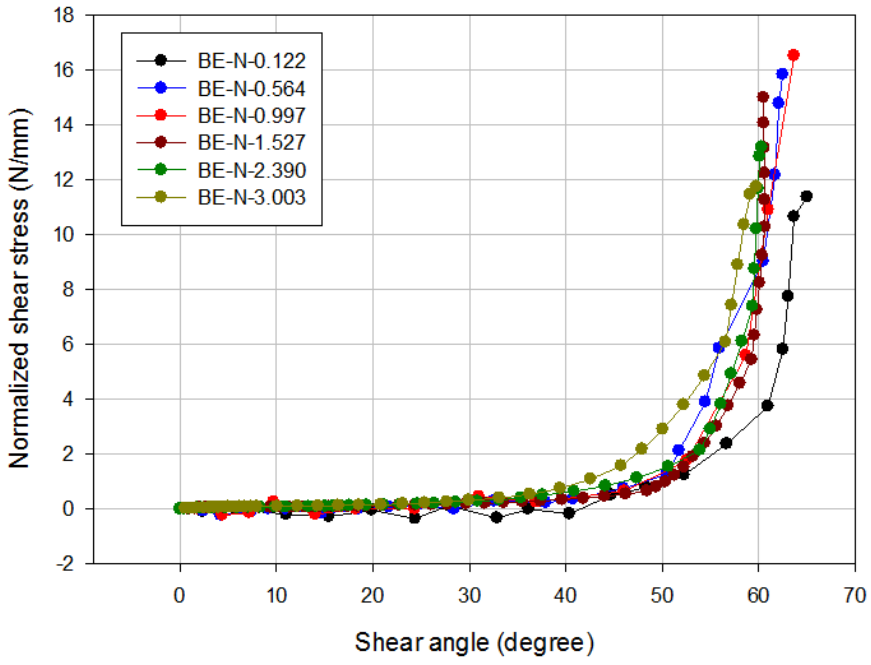


(a)

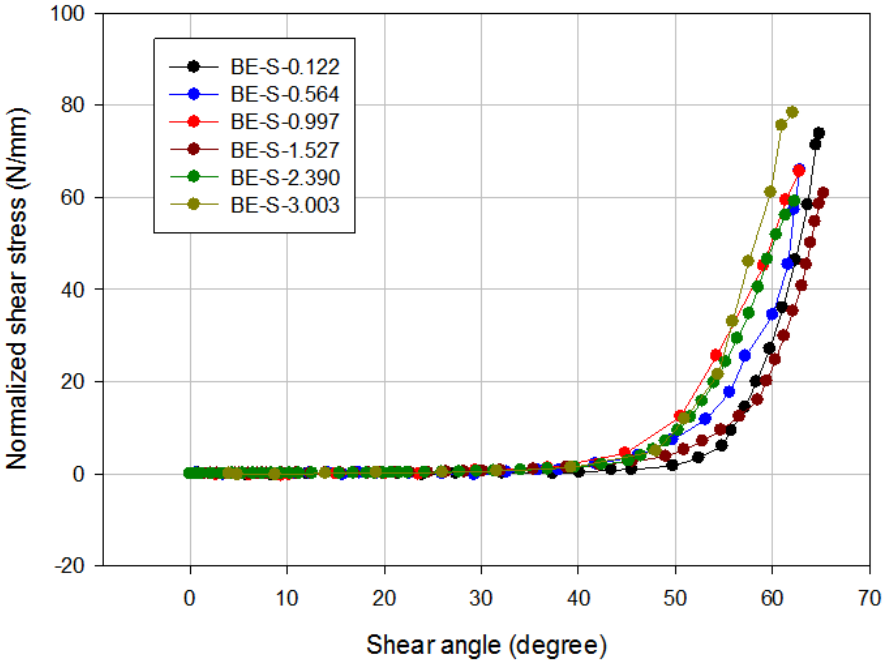


(b)

Figure 8. Shear stress vs. shear angle curves of the fabrics obtained from uniaxial BE tests. (a) Neat fabric and (b) STF-im-AR fabrics. The legends indicate the shear rate from 0.122-3.003 rad/s.

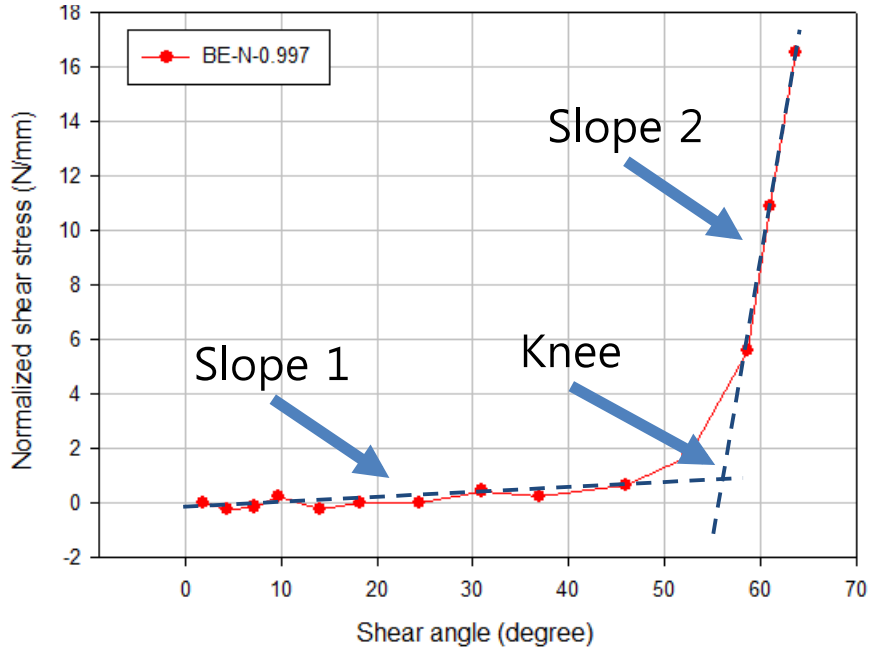
BE-N-0.997
Slope 2
Slope 1
Knee
Normalized shear stress (N/mm)
Shear angle (degree)
18
16
14
12
10
8
6
4
2
0
-2
0
10
20
30
40
50
60
70

(a)

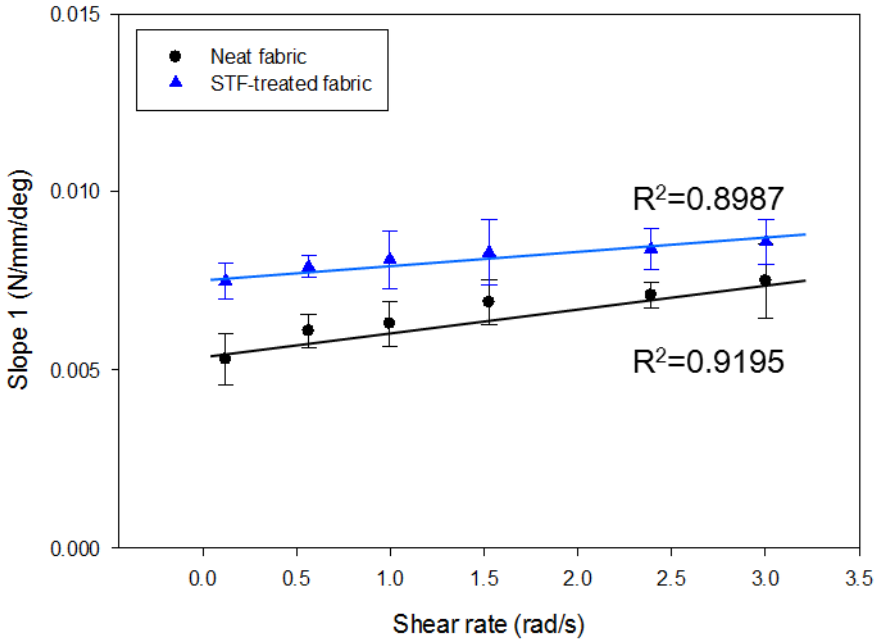
Neat fabric
STF-treated fabric
R2=0.8987
R2=0.9195
Slope 1 (N/mm/deg)
Shear rate (rad/s)
0.015
0.010
0.005
0.000
0.0
0.5
1.0
1.5
2.0
2.5
3.0
3.5

(b)

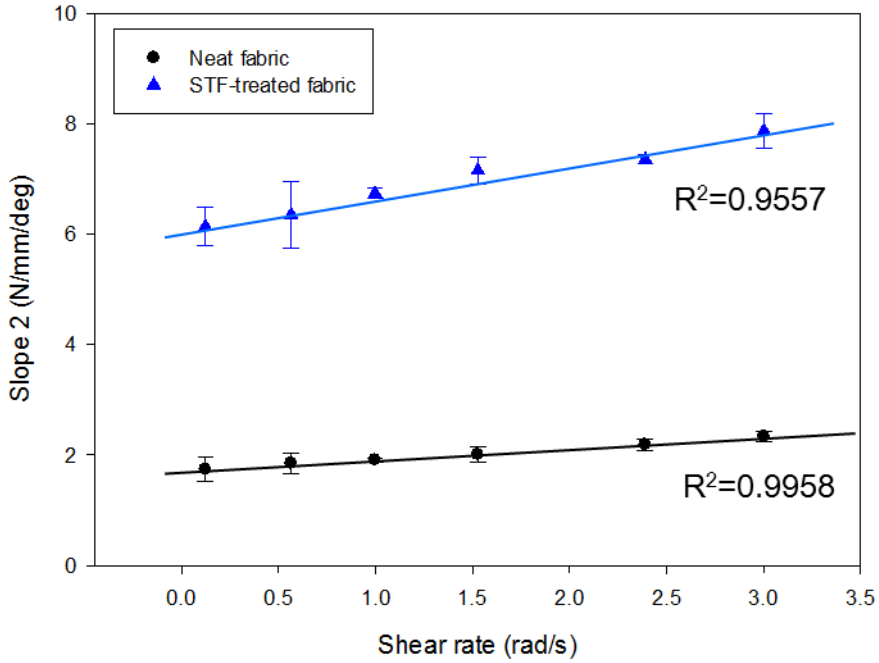


(c)

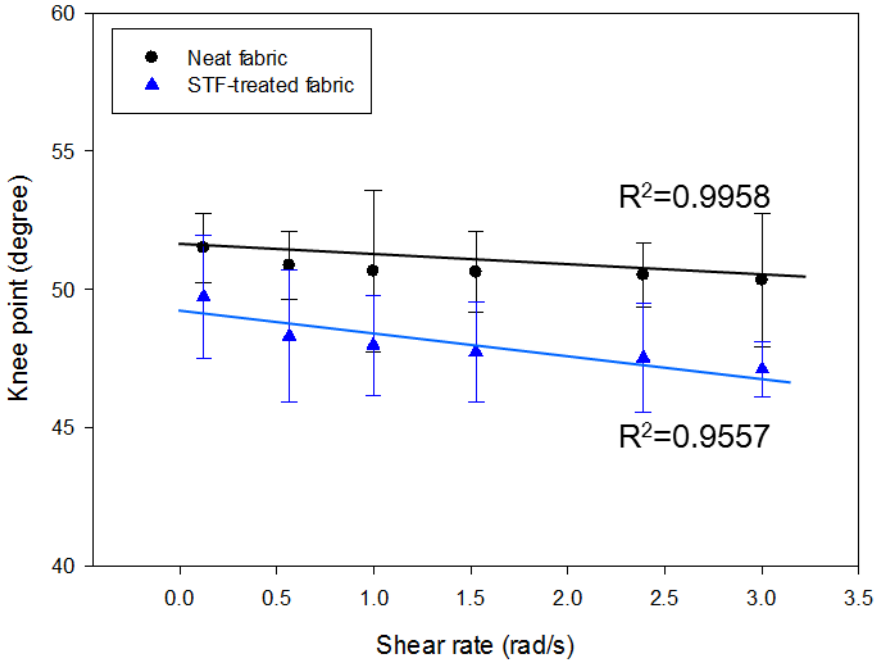


(d)

Figure 9. Representative shear properties of the neat and STF-impregnated fabrics measured by the BE test at different shear strain rates. (a) Bilinear approximations of the (a) normalized shear stress vs. shear angle, (b) Slope 1, (c) Slope 2, and (d) knee point as a function of the shear rate.

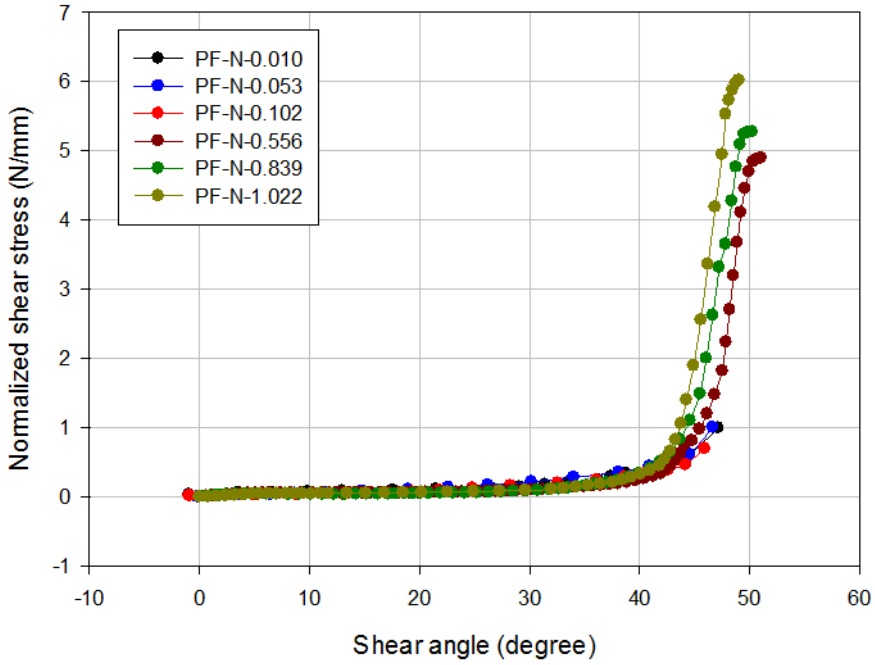


(a)

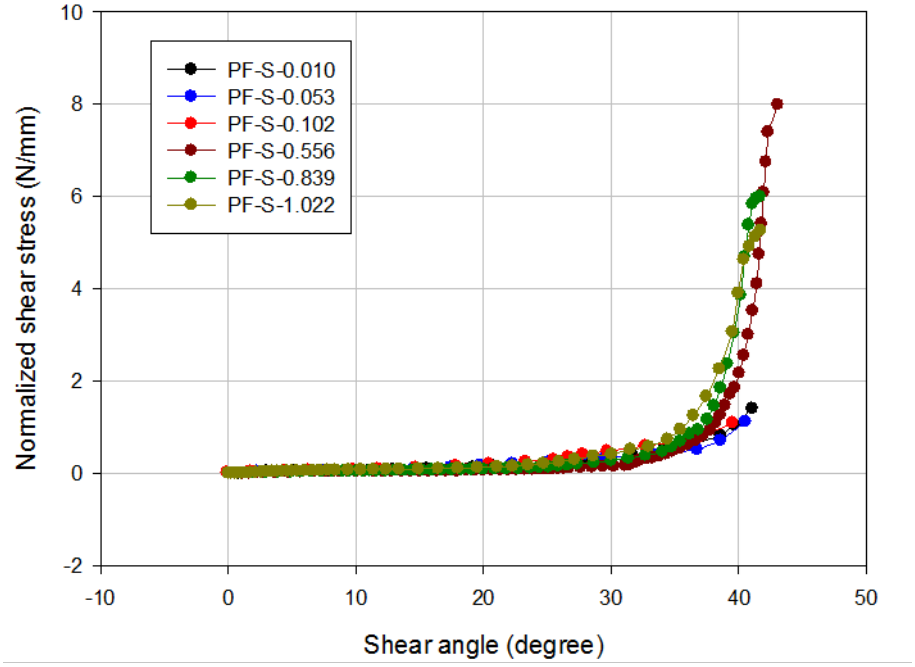


(b)

Figure 10. Normalized shear force vs. shear angle curves of the (a) Neat fabric and (b) STF-im-AR fabric measured using the PF test.

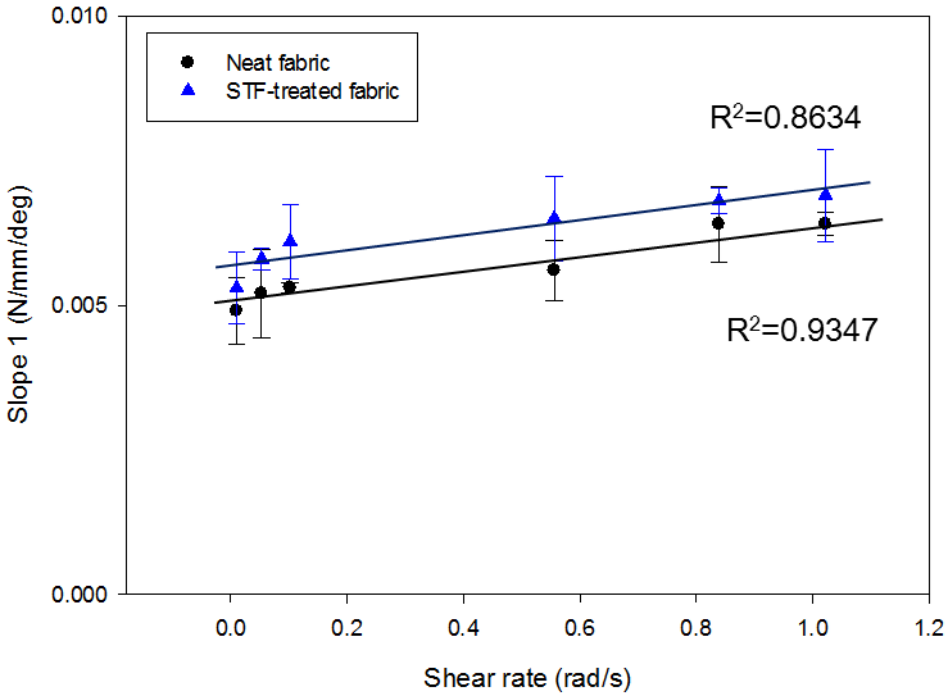
Neat fabric
STF-treated fabric
R2=0.8634
R2=0.9347
Slope 1 (N/mm/deg)
Shear rate (rad/s)
0.010
0.005
0.000
0.0
0.2
0.4
0.6
0.8
1.0
1.2

(a)

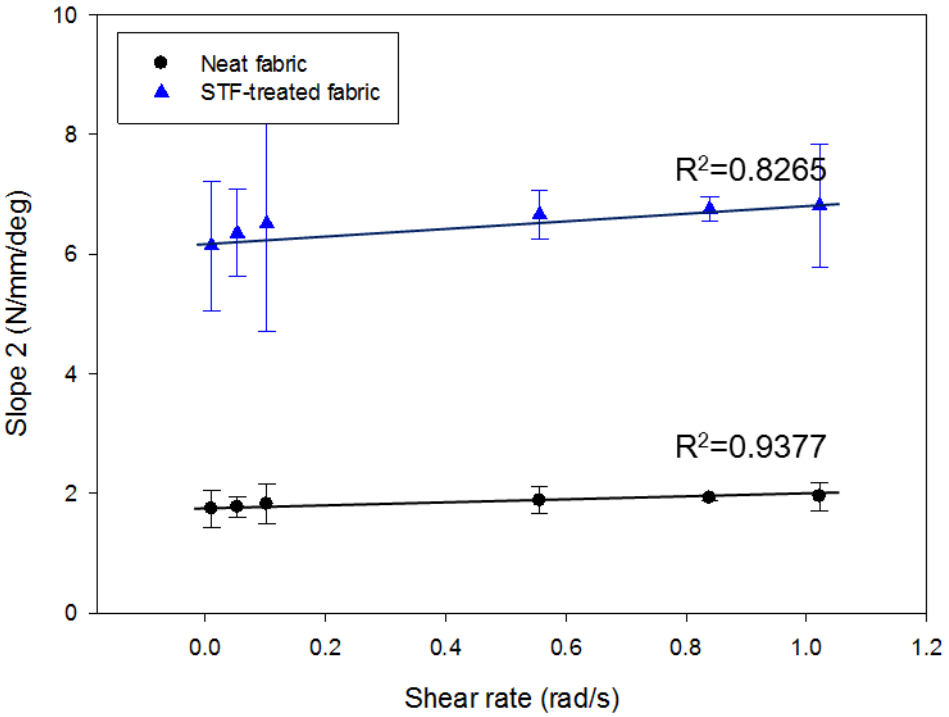
Neat fabric
STF-treated fabric
R2=0.8265
R2=0.9377
Slope 2 (N/mm/deg)
Shear rate (rad/s)
10
8
6
4
2
0
0.0
0.2
0.4
0.6
0.8
1.0
1.2

(b)

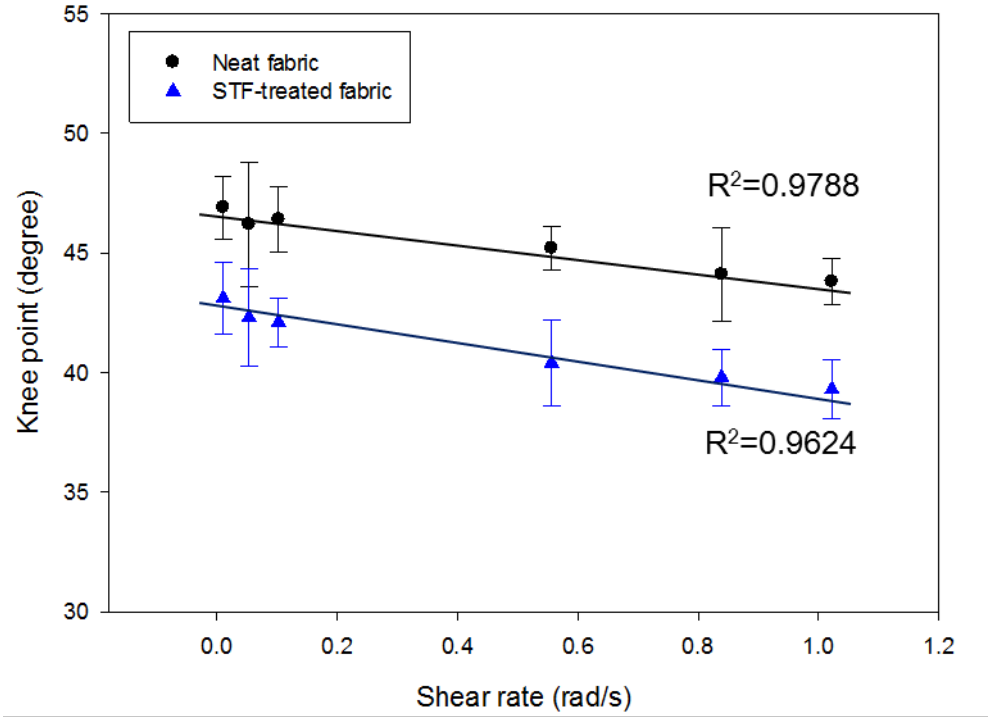


(c)

Figure 11. Representative bilinear shear properties of the neat and STF-impregnated aramid fabrics: (a) Slope 1, (b) Slope 2, and (c) knee angle as a function of shear rate.

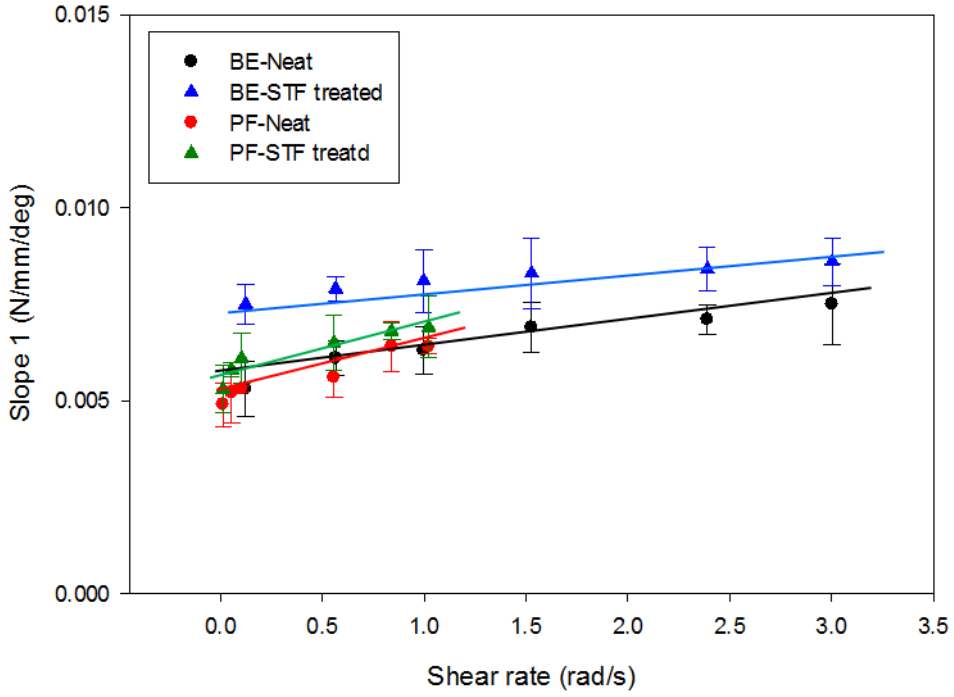
BE-Neat
BE-STF treated
PF-Neat
PF-STF treatd
Slope 1 (N/mm/deg)
0.015
0.010
0.005
0.000
0.0
0.5
1.0
1.5
2.0
2.5
3.0
3.5
Shear rate (rad/s)

(a)

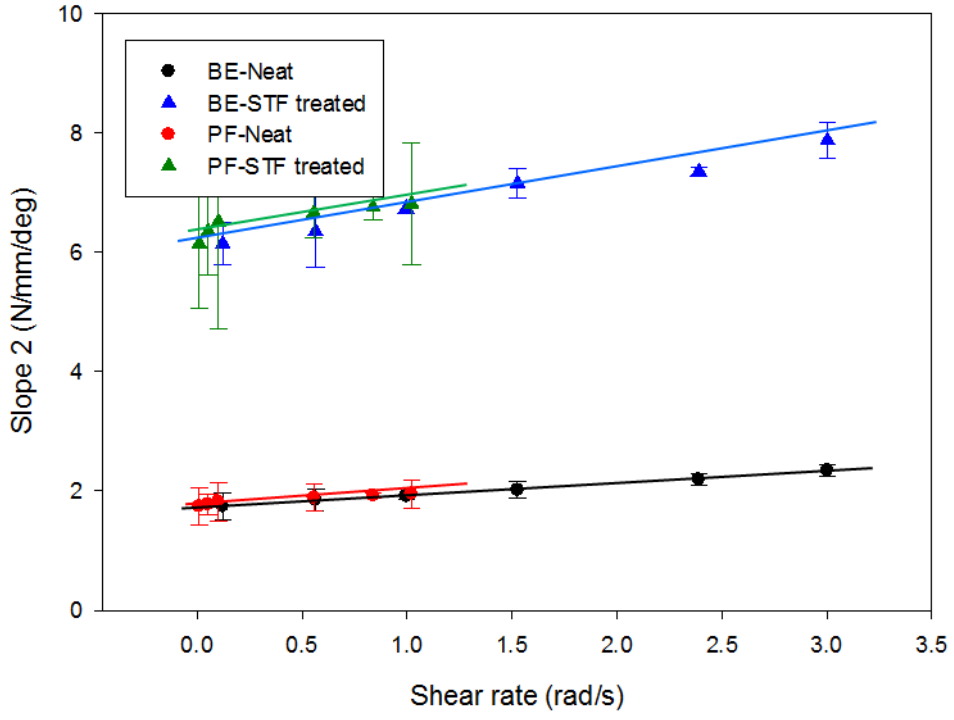
BE-Neat
BE-STF treated
PF-Neat
PF-STF treated
Slope 2 (N/mm/deg)
10
8
6
4
2
0
0.0
0.5
1.0
1.5
2.0
2.5
3.0
3.5
Shear rate (rad/s)

(b)

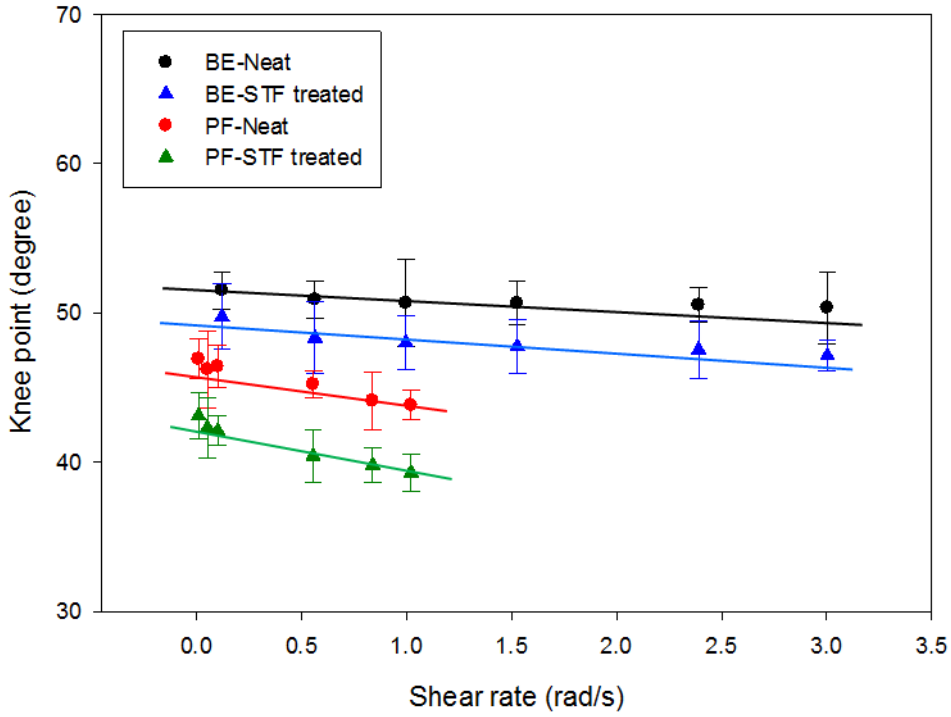


(c)

Figure 12. Comparison of the bilinear shear properties of the neat and STF-impregnated fabrics measured by the BE and PF tests: (a) Slope 1, (b) Slope 2, and (c) knee angle as a function of shear rate.